

Modeling three-dimensional crack propagation—A comparison of crack path tracking strategies

P. Jäger¹, P. Steinmann² and E. Kuhl^{3,*},†

¹*Department of Mechanical Engineering, University of Kaiserslautern, 67653 Kaiserslautern, Germany*

²*Department of Mechanical Engineering, Friedrich-Alexander University Erlangen-Nuremberg, 91058 Erlangen, Germany*

³*Department of Mechanical Engineering, Stanford University, Stanford, CA-94305, U.S.A.*

SUMMARY

The development of a new finite element technique for the simulation of discontinuous failure phenomena in three dimensions is the key objective of this study. In contrast to the widely used extended finite element technique, we apply a purely deformation-based strategy based on an independent interpolation of the deformation field on both sides of the discontinuity. This method has been applied successfully for two-dimensional crack propagation problems in the past. However, when it comes to three-dimensional failure phenomena, it faces the same difficulties as the extended finite element method. Unlike in two dimensions, the characterization for the three-dimensional failure surface is non-unique and the tracking of the discrete crack can be performed in several conceptually different ways. In this work, we review the four most common three-dimensional crack tracking strategies. We perform a systematic comparison in terms of standard algorithmic quality measures such as mesh independency, efficiency, robustness, stability and computational cost. Moreover, we discuss more specific issues such as crack path continuity and integratability in commercial finite element packages. The features of the suggested crack tracking algorithms will be elaborated by means of characteristic benchmark problems in failure analysis. Copyright © 2008 John Wiley & Sons, Ltd.

Received 17 September 2007; Revised 24 February 2008; Accepted 25 February 2008

KEY WORDS: three-dimensional crack propagation; fixed tracking; local tracking; global tracking; cohesive zone model; discrete failure

*Correspondence to: E. Kuhl, Department of Mechanical Engineering, Stanford University, Stanford, CA 94305-4040, U.S.A.

†E-mail: ekuhl@stanford.edu

Contract/grant sponsor: German National Science Foundation

1. MOTIVATION

The reliable prediction of crack propagation and failure of brittle materials and structures is an integral part in material design and structural analysis. In order to predict not only the failure load but also the post-peak behavior correctly, robust and stable computational algorithms that are capable of dealing with the highly non-linear set of governing equations are an essential requirement. Traditionally, finite element methods have been applied to model material failure in a smeared sense, i.e. continuous smooth failure was attributed to a softening stress–strain curve in the form of plasticity or damage on the element level. Discrete failure, however, was rather attributed to predefined interfaces that had to be introduced *a priori* as potential failure surfaces at selected inter-element boundaries. According to the cohesive zone concept, discrete failure was then collectively lumped into softening traction separation laws within the interface element.

The first method to truly simulate arbitrary discrete failure surfaces was the embedded discontinuity technique, see [1–6]. Motivated by the assumed enhanced strain concept, additional degrees of freedom were introduced locally on the element level to characterize the failure plane. The embedded discontinuity technique convinced through its computational efficiency: Due to the local nature of the enhancement, the size of the global system of equations was not effected by the newly introduced failure surface. An obvious drawback of the local crack representation, however, was the discontinuous nature of the failure surface that was soon found to introduce stress locking associated with an over-estimation of the structural stiffness. To overcome this deficiency, Belytschko and co-workers [7, 8] introduced a technique to successfully capture smooth failure surfaces: the celebrated extended finite element method. At the additional cost of successively introducing additional global degrees of freedom, smooth discrete cracks could finally be modeled anywhere in the domain, see also [9–13]. While Belytschko's extended finite element method uses the displacement jump as additional unknown, Hansbo's method advocated herein works exclusively with deformation degrees of freedom, see [14–19]. Based on a re-parameterization of unknowns, the latter shows certain advantages in combination with particular structural elements such as shells, see Areias and Belytschko [20], Areias *et al.* [21] or Jäger *et al.* [22].

For two-dimensional problems, both Belytschko's extended finite element method and Hansbo's method soon became popular to model concrete failure and brittle failure of composites, see [7–18, 22, 23]. In a two-dimensional setting, the tracking of crack propagation is rather straightforward. Once an element is identified to fail, typically decided based on a maximum principal stress criterion, the crack extends from a neighboring crack point on the element edge in the direction normal to the maximum principal stress. Although this stress-based crack propagation criterion always renders a unique and smooth C^0 -continuous failure zone in two-dimensional analyses, it eventually yields a non-smooth failure surface in a three-dimensional setting. Recent attempts in the literature have addressed the issue of crack propagation in three-dimensional failure analysis and a number of different strategies have been presented, see, e.g. [19, 22, 24–39]. This article addresses four of the most common approaches to track three-dimensional crack propagation and compares their algorithmic realization by means of common quality measures such as robustness, stability, efficiency, computational cost, mesh objectivity, generality and crack surface continuity.

The algorithm we discuss first is the fixed crack tracking scheme for which, similar to computations based on classical interface elements, the crack path has to be *a priori* known. This algorithm is thus pretty simple and boils down to deciding whether the stresses in the next element of the potential crack path exceed the critical failure stress and the element fails or rather remains continuous. From a computational point of view, this algorithm is particularly robust and stable.

A slightly more complicated scheme is the local crack tracking scheme, which can be interpreted as the three-dimensional generalization of crack tracking in two-dimensional failure analysis. Here, the crack essentially extends from neighboring crack points and proceeds in the direction normal to the maximum principal stress. As this concept would eventually render non-smooth surfaces, Areias and Belytschko [24] have suggested to adjust the crack plane normal based on neighboring crack intersection points. In the case of too many neighboring points, however, the system is over-determined and the crack hardly deviates from a planar surface. The structural stiffness might thus be severely overestimated.

A non-local crack tracking scheme is a successful means to remedy this deficiency. By averaging the crack plane normal over a certain neighborhood, Gasser and Holzapfel [27, 28] ensure that the generated failure surface is smooth in average, see also [29, 40]. However, as for all non-local averaging techniques, this concept is not really tailored to the modular element-wise nature of finite element analyses. Although theoretically elegant, it is rather cumbersome to include it into existing finite element codes as it affects not only the integration point and the element level but also the global structural level.

An extremely elegant and yet very powerful strategy that circumvents nearly all of the deficiencies above is the global crack tracking scheme introduced recently by Oliver and co-workers [25, 34, 41]. It provides a finite element-specific solution to the problem of kinematic crack characterization as it introduces an additional scalar-valued unknown that defines one or multiple crack surfaces as isosurfaces of this additional field of unknowns, see [26, 29, 42, 43]. Continuous smooth, planar or curved discontinuity surfaces can thus be described in a robust and stable manner, however, at the cost of having to solve an additional global system of equations within the post-processing step. Global crack tracking is not only by far the most general of all the four strategies, due to its modular nature, it can also be incorporated into existing finite element codes in an efficient and straightforward way.

In this article, we would like to share our experience and some of the sneaky tricks to successfully model crack propagation in three-dimensional domains. This article is organized as follows. Section 2 briefly summarizes the governing equations of a continuous body crossed by a discontinuity surface. In addition, it illustrates their finite element discretization based on a purely deformation-based Hansbo interpolation scheme. Sections 3–6 are organized in the same manner. They first introduce the algorithm of the individual crack tracking scheme and then provide an illustrative example. Section 3 discusses fixed crack tracking for which the potential failure surface has to be *a priori* known. Section 4 summarizes local crack tracking, which is a straightforward generalization of the algorithms typically applied in two-dimensional problems. Section 5 introduces non-local crack tracking based on a particular spatial averaging technique for the crack plane normal. Section 6 discusses global crack tracking based on solving an additional global system of equations defining the smooth and continuous crack surface. Section 8 then concludes with a critical discussion of all four schemes. Based on a systematic comparison, we try to give final advice and summarize which of the methods would be superior for particular subclasses of three-dimensional crack propagation phenomena.

2. SIMULATION OF CRACK PROPAGATION

To introduce the basic notation, we briefly discuss the governing equations for a continuous body \mathcal{B} crossed by a discontinuity Γ . For this type of problems, it proves convenient to introduce two

sets of equations, i.e. two kinematic, equilibrium and constitutive equations, one for the continuous body \mathcal{B} and one for the discontinuity surface Γ itself. These will be summarized in the sequel.

2.1. Kinematic equations

To ensure uniqueness of the kinematic description, the non-linear deformation ϕ mapping particles from their original position \mathbf{X} in the reference configuration \mathcal{B} to their current position \mathbf{x} in the deformed configuration \mathcal{S} is introduced independently on both sides of the discontinuity, \mathcal{B}^+ and \mathcal{B}^- , see Figure 1

$$\phi(\mathbf{X}) := \begin{cases} \phi^+(\mathbf{X}) \\ \phi^-(\mathbf{X}) \end{cases}, \quad \mathbf{F} = \begin{cases} \mathbf{F}^+ = \nabla_{\mathbf{X}}\phi^+ & \forall \mathbf{X} \in \mathcal{B}^+ \\ \mathbf{F}^- = \nabla_{\mathbf{X}}\phi^- & \forall \mathbf{X} \in \mathcal{B}^- \end{cases} \quad (1)$$

Accordingly, we can introduce independent deformation gradients \mathbf{F}^+ and \mathbf{F}^- and corresponding Jacobians $J^+ = \det(\mathbf{F}^+)$ and $J^- = \det(\mathbf{F}^-)$ on either side of the discontinuity. This parameterization inherently captures jumps $[[\phi]]$ in the deformation map, which obviously take the following straightforward representation $[[\phi]] = \phi^+ - \phi^- \quad \forall \mathbf{X} \in \Gamma$.

As illustrated in Figure 2, all particles initially located on the unique discontinuity surface Γ are mapped onto two surfaces γ^+ and γ^- in the deformed configuration. To uniquely characterize discontinuous failure at finite deformations, we apply the concept of a fictitious discontinuity $\bar{\phi}$, which is assumed to be located right between the two discontinuity surfaces γ^+ and γ^- in the deformed configuration

$$\bar{\phi} := \frac{1}{2}[\phi^+ + \phi^-], \quad \bar{\mathbf{F}} = \frac{1}{2}[\mathbf{F}^+ + \mathbf{F}^-] \quad \forall \mathbf{X} \in \Gamma \quad (2)$$

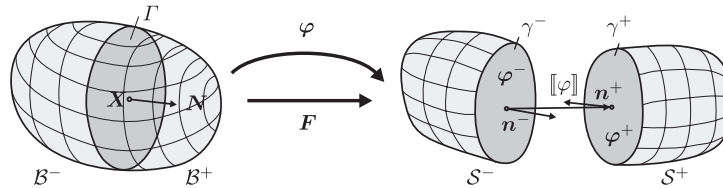


Figure 1. Kinematics—Independent mappings ϕ^+ and ϕ^- on both sides \mathcal{B}^+ and \mathcal{B}^- of the discontinuity Γ inherently introducing jump $[[\phi]]$ in the deformation field.

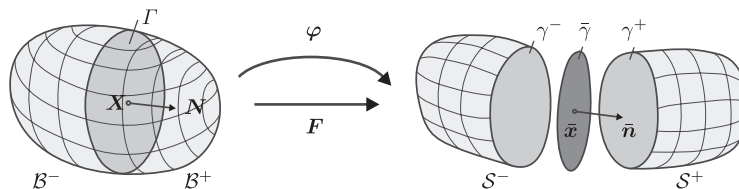


Figure 2. Kinematics—Concept of fictitious discontinuity surface $\bar{\gamma}$ located between the two discontinuity surfaces γ^+ and γ^- .

Again, the corresponding deformation gradient $\bar{\mathbf{F}}$ and its Jacobian $\bar{J} = \det \bar{\mathbf{F}}$ follow straightforwardly. The normal $\bar{\mathbf{n}}$ to the fictitious discontinuity that will essentially be needed to determine normal and shear resultants on the discontinuity $\bar{\gamma}$ can then be expressed through the classical Nanson formula as $\bar{\mathbf{n}} = \bar{J} \bar{\mathbf{F}}^{-t} \cdot \mathbf{N}$.

2.2. Equilibrium equations

In the absence of body forces and inertia terms, the equilibrium of external and internal forces requires that the divergence of the Piola stress \mathbf{P} with respect to the reference configuration vanishes identically in both subdomains \mathcal{B}^+ and \mathcal{B}^-

$$\text{Div}(\mathbf{P}) = \mathbf{0} \quad \forall \mathbf{X} \in \mathcal{B}^+ \cup \mathcal{B}^- \tag{3}$$

On the external boundary $\partial\mathcal{B}$, which can be subdivided into disjoint parts $\partial\mathcal{B} = \partial\mathcal{B}_u \cup \partial\mathcal{B}_t$ with $\partial\mathcal{B}_u \cap \partial\mathcal{B}_t = \emptyset$, either Dirichlet boundary conditions $\boldsymbol{\varphi} = \boldsymbol{\varphi}^p$ or Neumann boundary conditions $\mathbf{P} \cdot \mathbf{N} = \mathbf{T}^p$ can be prescribed. On the internal boundary Γ , i.e. along the fictitious discontinuity, the equilibrium condition

$$\mathbf{P}^+ \cdot \mathbf{N} = \mathbf{P}^- \cdot \mathbf{N} = \bar{\mathbf{T}} \quad \forall \mathbf{X} \in \Gamma \tag{4}$$

states that the cohesive tractions $\bar{\mathbf{T}}$ acting on the discontinuity have to be equal in direction and magnitude, however, taking the opposite sign, compare Figure 3.

2.3. Constitutive equations

We assume a compressible elastic constitutive behavior of Neo-Hooke type inside the bulk introducing the Cauchy stress $\boldsymbol{\sigma}$ in terms of the Lamé parameters λ and μ . The Cauchy or rather true stress $\boldsymbol{\sigma}$ can be related to the Piola stress \mathbf{P} through Nanson’s formula in a standard manner. Recall that the stress can generally take different values on both sides of the discontinuities \mathcal{B}^+ and \mathcal{B}^- .

$$\mathbf{P} = J \boldsymbol{\sigma} \cdot \mathbf{F}^{-t}, \quad \boldsymbol{\sigma} = \frac{1}{J} [\lambda \ln(J) \mathbf{I} - \mu \mathbf{I} + \mu \mathbf{F} \cdot \mathbf{F}^t] \quad \forall \mathbf{X} \in \mathcal{B}^+ \cup \mathcal{B}^- \tag{5}$$

The inelastic behavior is attributed exclusively to the fictitious discontinuity surface. We apply the cohesive crack concept, in which all inelastic deformations around the crack tip are collectively represented through the cohesive tractions $\bar{\mathbf{t}}$ on the discontinuity. Similar to the true stresses in the bulk, the true cohesive tractions $\bar{\mathbf{t}}$ can be related to the cohesive tractions $\bar{\mathbf{T}}$ on the undeformed

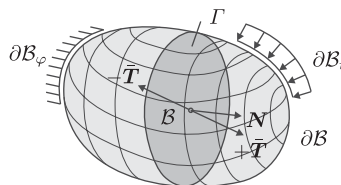


Figure 3. Boundary value problem of body \mathcal{B} with external boundary $\partial\mathcal{B}$ on which either Dirichlet boundary conditions $\boldsymbol{\varphi} = \boldsymbol{\varphi}^p$ or Neumann boundary conditions $\mathbf{P} \cdot \mathbf{N} = \mathbf{T}^p$ can be prescribed.

domain through Nanson’s formula in terms of area elements da and dA . We conveniently assume a decoupling of the normal and tangential constitutive behavior and introduce the true or rather Cauchy tractions $\bar{\mathbf{t}}$ in the following form:

$$\bar{\mathbf{T}} = \frac{da}{dA} \bar{\mathbf{t}}, \quad \bar{\mathbf{t}} = f_n \exp\left(-\frac{f_n}{G_n} [[\boldsymbol{\varphi}]] \cdot \bar{\mathbf{n}}\right) \bar{\mathbf{n}} + E_t [\mathbf{I} - \bar{\mathbf{n}} \otimes \bar{\mathbf{n}}] \cdot [[\boldsymbol{\varphi}]] \quad \forall \mathbf{X} \in \Gamma \tag{6}$$

In the normal direction, f_n and G_n denote the tensile strength and the fracture energy, respectively. In the tangential direction, E_t denotes the shear stiffness.

2.4. Weak form

After multiplication with the corresponding test functions $\delta\boldsymbol{\varphi}$ and $[[\delta\boldsymbol{\varphi}]]$, integration over the domain of interest, and inclusion of the Neumann boundary conditions, the equilibrium equations (3) and (4) render the weak form

$$\int_{\mathcal{B}^+ \cup \mathcal{B}^-} \delta\mathbf{F} : \mathbf{P} \, dV + \int_{\Gamma} [[\delta\boldsymbol{\varphi}]] \cdot \bar{\mathbf{T}} \, dA = \int_{\partial\mathcal{B}_t} \delta\boldsymbol{\varphi} \cdot \mathbf{T}^p \, dA \tag{7}$$

which essentially constitutes the basis for the finite element discretization to be discussed in the sequel.

2.5. Discretization

For the finite element formulation, it proves convenient to distinguish between standard continuous elements and discontinuous elements that are crossed by the discontinuity surface. For the continuous elements, we apply a standard interpolation of the test functions $\delta\boldsymbol{\varphi}$, the deformation field $\boldsymbol{\varphi}$, and their gradients $\delta\mathbf{F}$ and \mathbf{F}

$$\begin{aligned} \delta\boldsymbol{\varphi} &= \sum_{i=1}^{n_{en}} \delta\boldsymbol{\varphi}_i N^i, & \boldsymbol{\varphi} &= \sum_{j=1}^{n_{en}} \boldsymbol{\varphi}_j N^j \\ \delta\mathbf{F} &= \sum_{i=1}^{n_{en}} \delta\boldsymbol{\varphi}_i \otimes \nabla_{\mathbf{X}} N^i, & \mathbf{F} &= \sum_{j=1}^{n_{en}} \boldsymbol{\varphi}_j \otimes \nabla_{\mathbf{X}} N^j \end{aligned} \quad \forall \mathbf{X} \in \mathcal{B} \tag{8}$$

Here N^i and N^j are the standard shape functions for tetrahedral elements and n_{en} is the number of element nodes. For the discontinuous elements, we apply an independent interpolation of the deformation fields $\boldsymbol{\varphi}^+$ and $\boldsymbol{\varphi}^-$ and its gradients \mathbf{F}^+ and \mathbf{F}^- on the individual sides of the discontinuities \mathcal{B}^+ and \mathcal{B}^- . Conceptually speaking, both deformation fields $\boldsymbol{\varphi}^+$ and $\boldsymbol{\varphi}^-$ are interpolated over the entire element through the nodal values in terms of the standard basis functions N^i . To this end, double the degrees of freedom and introduce two sets of standard shape functions with n_{en}^+ nodes for the interpolation on one side of the discontinuity and n_{en}^- nodes for the other side. The interpolated fields are then set to zero on one side of the discontinuity, while they take their usual values on the other side. The jumps in the test function $[[\delta\boldsymbol{\varphi}]] = \sum_{i=1}^{n_{en}^+} \delta\boldsymbol{\varphi}_i^+ N^i - \sum_{i=1}^{n_{en}^-} \delta\boldsymbol{\varphi}_i^- N^i$ and in the displacement field $[[\boldsymbol{\varphi}]] = \sum_{j=1}^{n_{en}^+} \boldsymbol{\varphi}_j^+ N^j - \sum_{j=1}^{n_{en}^-} \boldsymbol{\varphi}_j^- N^j$ can then be expressed as the difference of the two continuous fields evaluated at the internal boundary Γ . The average deformation gradient on the fictitious discontinuity surface $\bar{\mathbf{F}} = \frac{1}{2} [\sum_{j=1}^{n_{en}^+} \boldsymbol{\varphi}_j^+ \otimes \nabla_{\mathbf{X}} N^j +$

$\sum_{j=1}^{n_{en}^-} \boldsymbol{\varphi}_j^- \otimes \nabla_{\mathbf{X}} N^j]$ follows accordingly

$$\begin{aligned} \llbracket \delta \boldsymbol{\varphi} \rrbracket &= \sum_{i=1}^{n_{en}^+ + n_{en}^-} \delta \boldsymbol{\varphi}_i \bar{N}^i, & \llbracket \boldsymbol{\varphi} \rrbracket &= \sum_{j=1}^{n_{en}^+ + n_{en}^-} \boldsymbol{\varphi}_j \bar{N}^j \\ \delta \bar{\mathbf{F}} &= \sum_{i=1}^{n_{en}^+ + n_{en}^-} \delta \boldsymbol{\varphi}_i \otimes \nabla_{\mathbf{X}} \bar{N}^i, & \bar{\mathbf{F}} &= \sum_{j=1}^{n_{en}^+ + n_{en}^-} \boldsymbol{\varphi}_j \otimes \nabla_{\mathbf{X}} \bar{N}^j \end{aligned} \quad \forall \mathbf{X} \in \Gamma \tag{9}$$

To unify the notation, we have rearranged the terms in the interpolation and introduced the set \bar{N} which consists of the element shape functions N evaluated at Γ multiplied by the corresponding algebraic sign. Accordingly, $\nabla_{\mathbf{X}} \bar{N}$ denotes the gradient of the shape functions N evaluated at Γ , weighted by the factor $\frac{1}{2}$. With the help of the above-introduced discretizations, the weak form of the governing equations (7) can be cast into the following discrete residual statement:

$$\mathbf{R}_I = \mathbf{A}_{e=1}^{n_{el}} \int_{\mathcal{B}_e \cup \mathcal{B}_d^{+,-}} \nabla_{\mathbf{X}} N^i \cdot \mathbf{P} \, dV + \int_{\bar{\Gamma}} \bar{N}^i \bar{\mathbf{T}}(\llbracket \boldsymbol{\varphi} \rrbracket) \, d\bar{A} - \int_{\partial \mathcal{B}_{te}} N^i \mathbf{T}^p \, dA \doteq \mathbf{0} \tag{10}$$

where the operator $\mathbf{A}_{e=1}^{n_{el}}$ denotes the assembly of all element contributions, i.e. the continuous and the discontinuous ones. The above residual statement is solved numerically by using an incremental iterative Newton–Raphson scheme. The solution to the underlying linearized system of equations $\mathbf{R}_I^{k+1} = \mathbf{R}_I^k + d\mathbf{R}_I \doteq \mathbf{0}$ with the iterative residual $d\mathbf{R}_I = \sum_{J=1}^{n_{np}} \mathbf{K}_{IJ} d\boldsymbol{\varphi}_J$ and the incremental stiffness matrix $\mathbf{K}_{IJ} = \partial \mathbf{R}_I / \partial \boldsymbol{\varphi}_J$ with

$$\begin{aligned} \mathbf{K}_{IJ} &= \mathbf{A}_{e=1}^{n_{el}} \int_{\mathcal{B}_e \cup \mathcal{B}_d^{+,-}} \nabla_{\mathbf{X}} N^i \cdot [\partial_{\mathbf{F}} \mathbf{P}] \cdot \nabla_{\mathbf{X}} N^j \, dV \\ &\quad + \int_{\bar{\Gamma}} \bar{N}^i [\partial_{\llbracket \boldsymbol{\varphi} \rrbracket} \bar{\mathbf{T}}] \bar{N}^j + \bar{N}^i [\partial_{\bar{\mathbf{F}}} \bar{\mathbf{T}}] \cdot \nabla_{\mathbf{X}} \bar{N}^j \, d\bar{A} \end{aligned} \tag{11}$$

renders the incremental update of the vector of unknowns $d\boldsymbol{\varphi}_J$. The terms in brackets, i.e. the second-, third- and fourth-order tensors $[\partial_{\llbracket \boldsymbol{\varphi} \rrbracket} \bar{\mathbf{T}}]$, $[\partial_{\bar{\mathbf{F}}} \bar{\mathbf{T}}]$, $[\partial_{\mathbf{F}} \mathbf{P}]$ depend on the choice of the constitutive equations for the stresses in the continuous body and for the tractions on the discontinuity surface. For the particular choice suggested in (5) and (6) they are given, e.g. in Mergheim *et al.* [19] or Jäger *et al.* [22]. Recall that due to the chosen discretization scheme, the number of global node points n_{np} , which consists of the standard nodes and the additional duplicated node points for the discontinuous elements, increases progressively during ongoing crack propagation.

2.6. Crack propagation

Following the classical principal stress-based Rankine criterion, we allow the crack to propagate if the largest eigenvalue $\max\{\lambda_i^\sigma\}$ of the Cauchy stress exceeds the critical failure stress σ^{crit} and thus $\phi^\sigma > 0$

$$\phi^\sigma = \max\{\lambda_i^\sigma\} - \sigma^{\text{crit}} > 0 \quad \text{with} \quad \boldsymbol{\sigma} = \sum_{i=1}^3 \lambda_i^\sigma \mathbf{n}_i^\sigma \otimes \mathbf{n}_i^\sigma \tag{12}$$

The related maximum principal stress direction $\mathbf{n}^\sigma(\max\{\lambda_i^\sigma\})$ and its pull back to the reference configuration $\mathbf{N}^\sigma = \bar{J}^{-1} \bar{\mathbf{F}}^t \cdot \mathbf{n}^\sigma$ will prove essential for the kinematic characterization of the discontinuity surface. Unfortunately, unlike in two dimensions, the kinematic description of the propagating failure surface is non-unique in the three-dimensional setting. In the following sections, we introduce and discuss the four most prominent strategies for tracking failure surfaces and determining the crack plane normal \mathbf{N}^{crk} in three-dimensional crack propagation problems.

Remark 1 (Non-local crack propagation criterion)

To avoid spurious crack path oscillations, the Rankine criterion (12) is typically not evaluated in terms of the local stress $\boldsymbol{\sigma}$. Instead a non-local averaging is applied and the eigenvalue problem is solved for the non-local stress $\tilde{\boldsymbol{\sigma}}$, see, e.g. Jirasek *et al.* [44]. In the discrete setting and for constant strain elements, $\tilde{\boldsymbol{\sigma}}$ can simply be calculated as the volume average stress $\tilde{\boldsymbol{\sigma}} = \sum_{j \in \mathcal{J}^\sigma} V_j \boldsymbol{\sigma}_j / \sum_{j \in \mathcal{J}^\sigma} V_j$. The volume average stress $\tilde{\boldsymbol{\sigma}}$ is evaluated in all elements within the set \mathcal{J}^σ . This set contains all elements in a sphere of a user-defined radius r_σ around the current potential cracking point.

3. FIXED TRACKING

The determination of the crack plane normal \mathbf{N}^{crk} is the key challenge the three-dimensional crack propagation algorithms have to face. Obviously, the tracking of a propagating discontinuity is significantly simplified when the failure surface is *a priori* known. Typical examples of predefined failure surfaces are welded interfaces between substructures of the same material or joining zones between two substantially different materials. In this class of problems, the crack plane normal \mathbf{N}^{crk} is kinematically specified and is thus independent of the current stress state. Accordingly, no particular algorithm to track the crack path is needed. A typical example is the classical peel test as illustrated in Figures 4 and 6 for the symmetric and non-symmetric case, respectively.

The material parameters have been chosen according to the related literature, i.e. the Lamé parameters are $\lambda = 2778 \text{ N/mm}^2$ and $\mu = 4167 \text{ N/mm}^2$, the tensile strength is $f_n = 200 \text{ N/mm}^2$, the fracture toughness for the symmetric and non-symmetric case is $G_n = 100 \text{ N/mm}$ and $G_n = 50 \text{ N/mm}$, respectively. For this particular example, we assume that the shear stiffness is negligible as $E_t = 0 \text{ N/mm}^2$.

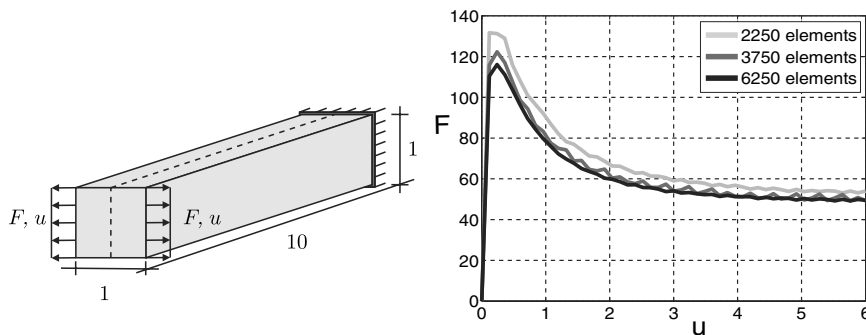


Figure 4. Symmetric peel test—Geometry and load displacement curves for fixed tracking algorithm.

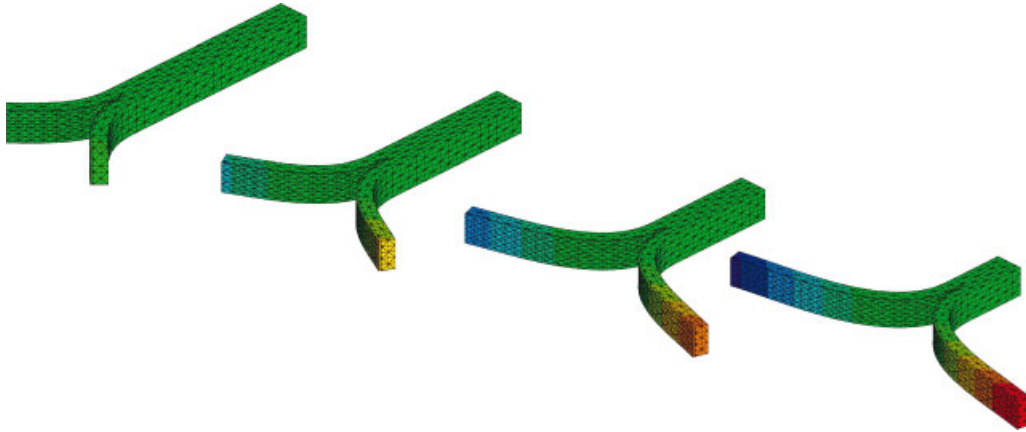


Figure 5. Symmetric peel test—Deformed configurations for load steps 25, 50, 75 and 100 for fixed tracking algorithm.

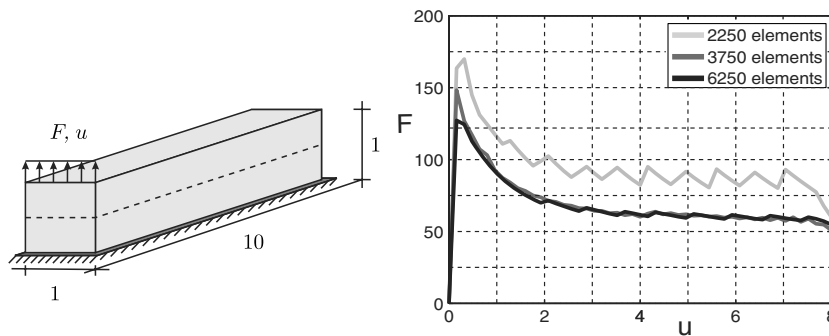


Figure 6. Non-symmetric peel test—Geometry and load displacement curves for fixed tracking algorithm.

Figure 5 illustrates a sequence of the crack propagation snapshots for the symmetric peeling of two identical layers discretized with 3750 linear tetrahedral elements. The smooth peeling of the two halves is clearly visible as the discontinuity progresses through the specimen. Figure 7 shows the simulation of the non-symmetric peel test for which we peel off the top layer of the specimen while its bottom layer is fixed. The non-symmetric peel test is particularly challenging as the fictitious discontinuity surface obviously undergoes significant rotations. Accordingly, although the crack plane normal \mathbf{N}^{crk} in the reference configuration is constant, $\mathbf{n}^{\text{crk}} = \bar{\mathbf{J}}\bar{\mathbf{F}}^{-t} \cdot \mathbf{N}^{\text{crk}}$ is not. This benchmark problem can thus be used to elaborate the correctness of the consistent linearization of the cohesive traction term. Similar to the previous example, the crack opens progressively and a smooth peeling process can be observed.

Figures 5 and 7 illustrate that the suggested algorithm is in principle capable to capture three-dimensional crack propagation phenomena. Another typical quality measure of crack simulation algorithms is the mesh independency of the numerical solution. Figures 4 and 6 display the load–deflection curves for both symmetric and non-symmetric peel tests each being discretized with 2250, 3750 and 6250 linear tetrahedral elements. Although the 2250 element meshes seem to

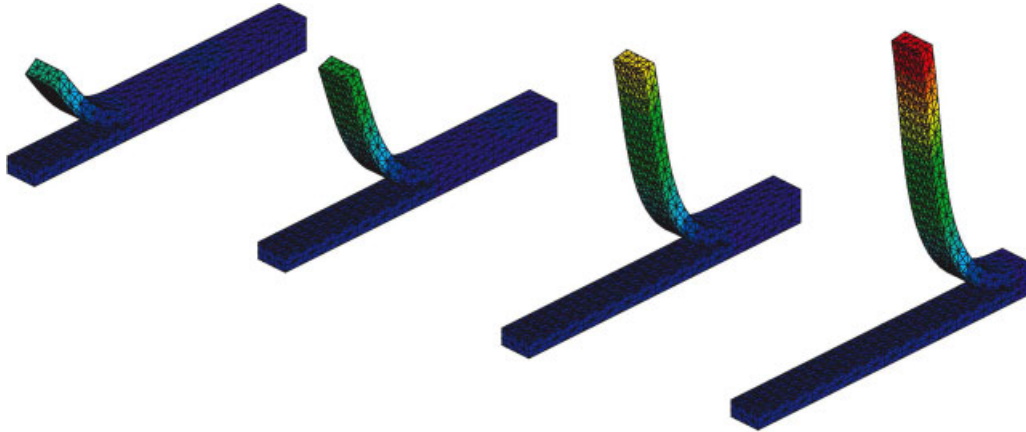


Figure 7. Non-symmetric peel test—Deformed configurations for load steps 25, 50, 75 and 100 for fixed tracking algorithm.

be too coarse to capture the failure process appropriately, the finer meshes of 3750 and 6250 elements render almost identical results. The ability to produce mesh-independent results is thus a distinguishing feature of the suggested algorithm. Although here, for both cases we expect a planar failure surface in the reference configuration with a constant crack plane normal \mathbf{N}^{crk} , curved or more complex failure surfaces can be prescribed in a similar manner at a rather moderate increase of algorithmic complexity.

Remark 2 (Continuity)

By its very nature, the fixed crack tracking algorithm is able to capture failure surfaces of any order of continuity. Nevertheless, the failure surface is typically approximated \mathcal{C}^0 -continuously.

Remark 3 (Computational cost)

As the crack path has to be known *a priori* for this algorithm, the computational cost is restricted to checking whether or not the crack propagates.

4. LOCAL TRACKING

Let us now turn to more challenging failure phenomena for which the failure surface is not *a priori* known. For these more complex problems, the crack plane normal \mathbf{N}^{crk} is a result of the loading history and thus part of the solution itself. In accordance with the linear interpolation of the deformation field, the three-dimensional failure surface is typically assumed to be element-wise planar. It can be characterized through a point in the plane and the crack plane normal \mathbf{N}^{crk} . In the following we shall elaborate the local crack tracking method that was initially proposed by Areias and Belytschko [24]. They suggest that \mathbf{N}^{crk} is essentially based on the maximum principal stress direction \mathbf{N}^{σ} introduced in Section 2.6; however, it is slightly modified depending on cracked neighboring elements. To some extent, this method is a natural generalization of the crack propagation algorithms that have successfully been applied in two-dimensional crack propagation. Let us assume that the current crack surface at time t_n is represented by n^{crk} crack points. These are

the element-wise intersection points \mathbf{C}_i of the element discontinuities and the element edges. As such, they represent the corners of the element-wise planar triangular or quadrilateral discontinuity plane. The number of crack neighbor points can vary between 0 and 4, i.e. $i \in \{0, 2, 3, 4\}$ and introduces six possible fundamentally different crack scenarios as illustrated in Figure 8.

Case I only occurs during crack initiation, i.e. $i = 0$. At initiation, the crack plane normal \mathbf{N}^{crk} is chosen to be identical to the direction of maximum tensile stress \mathbf{N}^σ . Case II corresponds to one single cracked neighbor element, i.e. $i = 2$. In this case, the new crack plane normal \mathbf{N}^{crk} depends on both the initial crack geometry \mathbf{C}_i and the direction of maximum tensile stress \mathbf{N}^σ . Cases III–VI are entirely determined by the three or four given neighboring crack points \mathbf{C}_i , i.e. $i = 3, 4$. The crack plane normal \mathbf{N}^{crk} then depends exclusively on the previous crack geometry and is completely independent of the maximum principal stress direction \mathbf{N}^σ . The element-wise definition of the new normal to the discontinuity \mathbf{N}^{crk} for all six cases is summarized in Table I. From the given definitions, it is obvious that \mathbf{N}^{crk} is not necessarily a unit vector. Note that during a standard crack propagation simulation cases II and III occur most frequently.

Remark 4 (Continuity)

The major drawback of the local tracking scheme is that it is severely restrictive by construction as the new crack plane normal \mathbf{N}^{crk} might eventually be fully determined by the previous crack geometry. Provided that this restriction is not violated; however, the algorithm generates perfectly smooth \mathcal{C}^0 -continuous discontinuity surfaces at extremely low computational cost. Typical examples in which the local tracking scheme has been proven successful are planar or slightly kinked discontinuity surfaces.

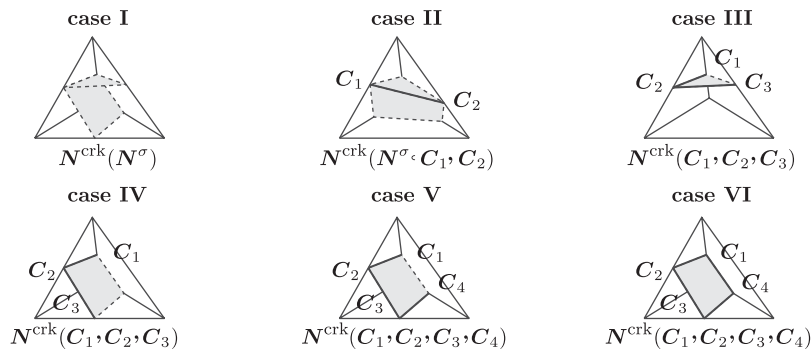


Figure 8. Local tracking—Illustration of crack scenarios I–VI, corresponding crack neighbor points \mathbf{C}_i and dependencies of crack plane normal \mathbf{N}^{crk} .

Table I. Local tracking—Summary of crack scenarios I–VI, definition of crack plane normal \mathbf{N}^{crk} .

Case	Crack	Normal	Determined by	Normal to discontinuity surface
I	Initiation	$\mathbf{N}^{\text{crk}}(\mathbf{N}^\sigma)$	Stress	$\mathbf{N}^{\text{crk}} = \mathbf{N}^\sigma$
II	Propagation	$\mathbf{N}^{\text{crk}}(\mathbf{N}^\sigma, \mathbf{C}_i)$	Stress and crack geometry	$\mathbf{N}^{\text{crk}} = \left[\mathbf{I} - \frac{[\mathbf{C}_1 - \mathbf{C}_2] \otimes [\mathbf{C}_1 - \mathbf{C}_2]}{ \mathbf{C}_1 - \mathbf{C}_2 ^2} \right] \cdot \mathbf{N}^\sigma$
III–VI	Propagation	$\mathbf{N}^{\text{crk}}(\mathbf{C}_i)$	Crack geometry	$\mathbf{N}^{\text{crk}} = [\mathbf{C}_1 - \mathbf{C}_2] \times [\mathbf{C}_3 - \mathbf{C}_2]$

Remark 5 (Computational cost)

Assume that the dynamic list of crack tip elements contains n^{tip} entries. Moreover, each tetrahedral element has four neighboring elements that are identified and stored in a neighbor list at the initialization of the mesh. The computational effort of this algorithm is thus remarkably small. In fact, it is restricted to looping over the four neighboring elements of all elements in the cracked element list.

5. NON-LOCAL TRACKING

An alternative strategy that successfully circumvents the limitations of the local tracking scheme has been introduced by Gasser and Holzapfel [27, 28], see also Gasser [29] and Feist and Hofstetter [40]. The non-local tracking algorithm is essentially based on a least-squares fit to extend the existing crack surface as smoothly as possible. To this end, the crack plane normal \mathbf{N}^{crk} calculated from the maximum principal stress direction \mathbf{N}^σ is not only adapted to the crack points \mathbf{C}_i of the neighboring elements as described in Section 4 for the local tracking scheme. Rather, it additionally accounts for the information of the set of all $n^{crk} = \dim(\mathcal{J}^{crk})$ crack points of the set $\mathcal{J}^{crk} = \{i \in \{1, \dots, n^{crk}\} | r_i < r^{crk}\}$ within a sphere of radius r^{crk} around the center $\bar{\mathbf{P}}$ of the currently analyzed element. Here, $r_i = |\mathbf{C}_i - \bar{\mathbf{P}}|$ obviously denotes the distance of the i th crack point \mathbf{C}_i from the current element center $\bar{\mathbf{P}}$. We assume that the position vectors \mathbf{C}_i for $i = 1, \dots, n^{crk}$ are given relative to a global cartesian coordinate system $\{X, Y, Z\}$ with the orthonormal base vectors $\mathbf{E}_1, \mathbf{E}_2, \mathbf{E}_3$.

The set of points \mathcal{J}^{crk} forms a point cloud with the geometric center $\mathbf{C}_c = 1/n^{crk} \sum_{i \in \mathcal{J}^{crk}} \mathbf{C}_i$. The orientation of this point cloud is given through a local second cartesian coordinate system $\{\bar{X}, \bar{Y}, \bar{Z}\}$ which is characterized by a second set of orthonormal base vectors $\bar{\mathbf{E}}_1, \bar{\mathbf{E}}_2, \bar{\mathbf{E}}_3$, see Figure 9. These orthonormal base vectors are the principal axes of the point cloud \mathcal{J}^{crk} . They can be determined as the eigenvectors of the covariance tensor Σ

$$\Sigma = \sum_{i=1}^3 \lambda_i^\Sigma \bar{\mathbf{E}}_i \otimes \bar{\mathbf{E}}_i \quad \text{with} \quad \Sigma = \sum_{i \in \mathcal{J}^{crk}} [\mathbf{C}_i - \mathbf{C}_c] \otimes [\mathbf{C}_i - \mathbf{C}_c] \tag{13}$$

Next we compute the crack point position vectors $\bar{\mathbf{C}}_i = \mathbf{C}_i - \mathbf{C}_c$ with respect to the point cloud center \mathbf{C}_c and transform the components of the corner point position vectors $[\bar{\mathbf{C}}_i]$ from the global coordinate system $\{X, Y, Z\}$ to the local coordinate system $\{\bar{X}, \bar{Y}, \bar{Z}\}$ with the help of the orthogonal transformation tensor $\mathbf{Q} = \sum_{i=1}^3 \bar{\mathbf{E}}_i \otimes \mathbf{E}_i$. Now the main idea of Gasser and Holzapfel [28] is to assume that the crack surface can be represented by a linear function in the local coordinate system

$$\bar{Z} = a_0 + a_1 \bar{X} + a_2 \bar{Y} \tag{14}$$

The coefficients a_0, a_1, a_2 in the local coordinate system follow from solving the corresponding least-squares problem, which reduces to the following symmetric system of linear equations:

$$\sum_{i \in \mathcal{J}^c} [\bar{Z}_i - \bar{Z}(a_j; \bar{X}_i, \bar{Y}_i)]^2 \rightarrow \min \sum_{i \in \mathcal{J}^c} \begin{bmatrix} 1 & \bar{X}_i & \bar{Y}_i \\ \bar{X}_i & \bar{X}_i^2 & \bar{X}_i \bar{Y}_i \\ \bar{Y}_i & \bar{X}_i \bar{Y}_i & \bar{Y}_i^2 \end{bmatrix} \begin{bmatrix} a_0 \\ a_1 \\ a_2 \end{bmatrix} = \sum_{i \in \mathcal{J}^c} \begin{bmatrix} \bar{Z}_i \\ \bar{X}_i \bar{Z}_i \\ \bar{Y}_i \bar{Z}_i \end{bmatrix} \tag{15}$$

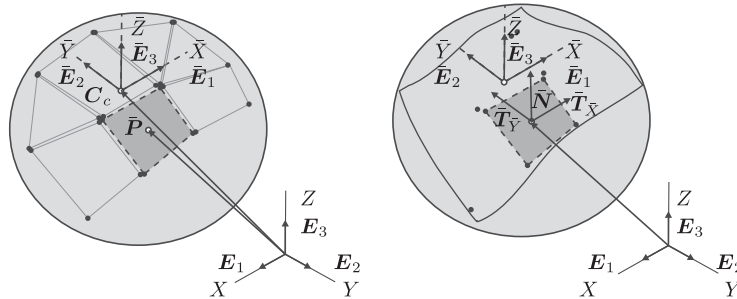


Figure 9. Non-local tracking—Normal averaging sphere around the crack tip $\bar{\mathbf{P}}$ introducing the set \mathcal{S}^{crk} of n^{crk} crack intersection points within the sphere. Element-wise planar crack surface defined through local tangential vectors $\bar{\mathbf{T}}_{\bar{X}}$ and $\bar{\mathbf{T}}_{\bar{Y}}$.

By construction, this element crack surface fits the existing crack nodes $\bar{\mathbf{C}}_i$ in a least-squares sense. The coefficients a_0, a_1, a_2 uniquely determine a smooth parametric representation of the crack surface. We compute the local representation of the crack plane normal $\bar{\mathbf{N}}$ in terms of the two tangent vectors $\bar{\mathbf{T}}_{\bar{X}}$ and $\bar{\mathbf{T}}_{\bar{Y}}$, which can be calculated straightforwardly as $\bar{\mathbf{Z}}$ is always perpendicular to that crack surface

$$\bar{\mathbf{N}}^{\text{crk}} = \bar{\mathbf{T}}_{\bar{X}} \times \bar{\mathbf{T}}_{\bar{Y}}, \quad \begin{aligned} \bar{\mathbf{T}}_{\bar{X}} &= \bar{\mathbf{E}}_1 + \partial_{\bar{X}} \bar{\mathbf{Z}} \bar{\mathbf{E}}_3 \\ \bar{\mathbf{T}}_{\bar{Y}} &= \bar{\mathbf{E}}_2 + \partial_{\bar{Y}} \bar{\mathbf{Z}} \bar{\mathbf{E}}_3 \end{aligned} \quad (16)$$

Finally, we transform the components $[\bar{\mathbf{N}}^{\text{crk}}]$ back from the local coordinate system $\{\bar{X}, \bar{Y}, \bar{Z}\}$ to the global coordinate system $\{X, Y, Z\}$ with the help of the orthogonal transformation tensor \mathbf{Q} .

Remark 6 (Continuity)

Note that although the failure surface is fitted in a least-squares sense for each element, the overall surface representation might eventually be non-smooth, i.e. by construction, the discontinuity surface \mathbf{N}^{crk} is only \mathcal{C}^{-1} -continuous. The smoothing radius r^{crk} takes the interpretation of a weighting parameter between the maximum principal stress direction \mathbf{N}^σ on the one hand and the existing crack kinematics \mathbf{C}_i on the other hand.

Remark 7 (Computational cost)

Again, we assume that all n^{tip} crack tip elements are stored in a dynamic crack tip list. For each crack tip element, we need to evaluate the point set \mathcal{S}^{crk} within the corresponding sphere of radius r^{crk} . Technically, this set can be calculated and stored once when the mesh is initialized. Then, at each step, a 3×3 system needs to be solved for each of the n^{tip} elements. The computational effort is thus larger than for the previous local tracking algorithm but yet significantly smaller than for the global tracking algorithm to be discussed in the following section. However, from our personal experience, the non-local tracking algorithm is rather cumbersome and the complexity of its implementation is relatively high.

Remark 8 (Crack deviation angle)

For computational reasons, it proves reasonable to ensure that the crack plane normals \mathbf{N}^{crk} between neighboring elements do not exceed a critical crack deviation angle. This restriction is of purely

algorithmic nature. It has been applied successfully for both local and non-local crack tracking algorithms in order to avoid spurious zick-zack-type crack surfaces.

Remark 9 (Non-local averaging)

As for every non-local averaging scheme, the quality of the averaging procedure strongly relies on the number of crack points n^{crk} within the averaging set \mathcal{I}^{crk} . A minimum amount of points is essential for the solution of the least-squares problem (15) which in turn crucially influences the quality of the crack tracking algorithm itself. Especially, at the onset of cracking, when the number of averaging points is rather limited, it seems reasonable to turn off the averaging mechanism and only switch it on when a sufficiently large number of data points n^{crk} are available. Then, one could even think of interpolating the element-wise failure surface through a quadratic rather than a linear approach at only very little extra cost as shown by Gasser and Holzapfel [27, 28].

6. GLOBAL TRACKING

To ensure a unique \mathcal{C}^0 -continuous representation of the discontinuity surfaces in three-dimensional crack propagation problems, Oliver and Huespe [34] and Oliver *et al.* [41] have proposed a robust and yet very elegant strategy that can be incorporated into commercial finite element codes in a remarkably efficient manner. Their initial idea has adopted successfully to simulate discrete fracture by Chaves [25], Feist and Hoffstetter [26, 45], Dumstorff and Meschke [43] and Cervera and Chiumenti [42]. The key feature of Oliver’s global tracking algorithm is to provide isosurfaces \mathcal{I}^ϕ which in the discrete setting take the interpretation of element-wise planar isopatches. These patches can be described by a function $\phi(\mathbf{X})$ whose level contours, i.e. the collection of all patches of $\phi(\mathbf{X}) = \phi_{\mathcal{I}^\phi} = \text{const}$, define the corresponding isosurface $\mathcal{I}^\phi = \{\mathbf{X} \in \mathcal{B} \mid \phi(\mathbf{X}) = \phi_{\mathcal{I}^\phi}\}$. A particular isosurface of constant value, e.g. the surface of level zero $\phi(\mathbf{X}) = 0$, is the kinematic representation of the discrete three-dimensional failure surface. Conceptually speaking, the ultimate goal of the algorithm is to find the scalar field $\phi(\mathbf{X})$ whose level surfaces are envelopes of the patches defined by the vectors $\mathbf{T}_{\bar{x}}$ and $\mathbf{T}_{\bar{y}}$ tangential to the propagating discontinuity. Similar to the previous non-local tracking strategy of Section 5, these tangents to the discontinuity surface, here represented in the global coordinate system, obviously obey the orthogonality condition $\mathbf{T}_{\bar{x}} \cdot \mathbf{N}^{crk} = 0$ and $\mathbf{T}_{\bar{y}} \cdot \mathbf{N}^{crk} = 0$ or rather $\mathbf{N}^{crk} = \mathbf{T}_{\bar{x}} \times \mathbf{T}_{\bar{y}}$. More importantly, by construction, these patches are always orthogonal to the gradient of the isosurface $\phi(\mathbf{X})$, thus $\mathbf{T}_{\bar{x}} \cdot \nabla \phi = 0$ and $\mathbf{T}_{\bar{y}} \cdot \nabla \phi = 0$. The multiplication of these conditions with $\mathbf{T}_{\bar{x}}$ and $\mathbf{T}_{\bar{y}}$, respectively, motivates the introduction of a flux vector $\mathbf{j} = [\mathbf{T}_{\bar{x}} \otimes \mathbf{T}_{\bar{x}} + \mathbf{T}_{\bar{y}} \otimes \mathbf{T}_{\bar{y}}] \cdot \nabla \phi$. A reinterpretation of the above considerations in terms of the classical field equations defines an equilibrium equation as the vanishing divergence of this flux vector \mathbf{j}

$$\text{Div}(\mathbf{j}) = \mathbf{0} \quad \forall \mathbf{X} \in \mathcal{B} \tag{17}$$

and a constitutive equation with the flux being a linear function of the gradient of $\nabla \phi$

$$\mathbf{j} = \mathbf{D} \cdot \nabla_X \phi \quad \forall \mathbf{X} \in \mathcal{B} \tag{18}$$

The particular format for the anisotropic constitutive tensor \mathbf{D}

$$\mathbf{D} = \mathbf{T}_{\bar{x}} \otimes \mathbf{T}_{\bar{x}} + \mathbf{T}_{\bar{y}} \otimes \mathbf{T}_{\bar{y}} \tag{19}$$

ensures that the flux is restricted to the $\{\bar{X}, \bar{Y}\}$ -plane, i.e. it is always a weighted linear combination of the tangent vectors $\mathbf{T}_{\bar{X}}$ and $\mathbf{T}_{\bar{Y}}$. The problem of finding isosurfaces \mathcal{I}^ϕ is obviously a classical boundary value problem in terms of the field ϕ characterized through an anisotropic Laplace-type equation. On the boundary $\partial\mathcal{B}$ which can be subdivided into disjoint parts $\partial\mathcal{B} = \partial\mathcal{B}_\phi \cup \partial\mathcal{B}_j$ with $\partial\mathcal{B}_\phi \cap \partial\mathcal{B}_j = \emptyset$ either Dirichlet boundary conditions $\phi = \phi^p$ or Neumann boundary conditions $\mathbf{j} \cdot \mathbf{N} = j^p$ can be prescribed, see Figure 10. Typically, we assume a flux-free boundary and apply homogeneous Neumann boundary conditions $\mathbf{j}^p \cdot \mathbf{N} = j^p = 0$. By multiplication with the test functions $\delta\phi$, integration over the domain \mathcal{B} , and inclusion of the Neumann boundary conditions $\mathbf{j} \cdot \mathbf{N} = j^p$, the equilibrium equation (17) can be cast into the following weak form:

$$\int_{\mathcal{B}} \nabla_{\mathbf{X}} \delta\phi \cdot \mathbf{D} \cdot \nabla_{\mathbf{X}} \phi \, dV = \int_{\partial\mathcal{B}_j} \delta\phi j^p \, dA \tag{20}$$

Similar to the deformation problem, we apply a standard linear interpolation of the test and trial functions $\delta\phi$ and ϕ and their gradients $\nabla_{\mathbf{X}} \delta\phi$ and $\nabla_{\mathbf{X}} \phi$

$$\begin{aligned} \delta\phi &= \sum_{i=1}^{n_{en}} \delta\phi_i N^i, & \phi &= \sum_{j=1}^{n_{en}} \phi_j N^j \\ \nabla_{\mathbf{X}} \delta\phi &= \sum_{i=1}^{n_{en}} \delta\phi_i \otimes \nabla_{\mathbf{X}} N^i, & \nabla_{\mathbf{X}} \phi &= \sum_{j=1}^{n_{en}} \phi_j \otimes \nabla_{\mathbf{X}} N^j \end{aligned} \quad \forall \mathbf{X} \in \mathcal{B} \tag{21}$$

The linear interpolation of $\phi(\mathbf{X})$ implies that the discrete isosurfaces \mathcal{I}^ϕ take an element-wise planar representation similar to the failure surfaces in the local and non-local tracking schemes of Sections 4 and 5. Once the discrete global linear system of equations

$$\mathbf{R}_I = \sum_{J=1}^{n_{np}} \mathbf{K}_{IJ} \phi_J, \quad \mathbf{R}_I = \mathbf{A} \int_{\partial\mathcal{B}_{je}} N^i j^p \, dA, \quad \mathbf{K}_{IJ} = \mathbf{A} \int_{\mathcal{B}_e} \nabla_{\mathbf{X}} N^i \cdot \mathbf{D} \cdot \nabla_{\mathbf{X}} N^j \, dV \tag{22}$$

is solved for the unknown field ϕ , the normal to the discontinuity surface \mathbf{N}^{crk} follows from a straightforward post-processing procedure on the element level.

Remark 10 (Continuity)

As this global tracking algorithm introduces the discrete crack in terms of the scalar isosurface value ϕ on the global level, its failure surface representation is inherently \mathcal{C}^0 -continuous, however, at the price of having to solve an additional global system of equations.

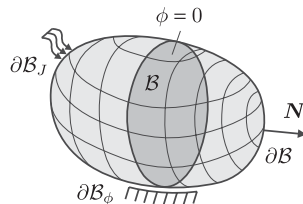


Figure 10. Global tracking—Boundary value problem of body \mathcal{B} with external boundary $\partial\mathcal{B}$ on which either Dirichlet boundary conditions $\phi = \phi^p$ or Neumann boundary conditions $\mathbf{j} \cdot \mathbf{N} = j^p$ can be prescribed.

Remark 11 (Computational cost)

The global tracking algorithm essentially relies on the assembly and solution to an additional global system of equations with one degree of freedom per node. In addition, a neighbor list needs to be initialized *ab initio* to evaluate average crack tip element values. The total computational cost of this algorithm is therefore the highest of all four algorithms discussed in this article. However, the global crack tracking algorithm is also the most flexible and also the most stable of all four algorithms. Note that due to its modular nature, its implementation in commercial finite element codes is rather straightforward.

Remark 12 (Boundary conditions)

As the global crack tracking scheme introduces an additional field of unknowns ϕ , additional boundary conditions have to be prescribed. To guarantee the invertibility of the system matrix the level of the isosurfaces ϕ has to be prescribed at least at two points. The physical interpretation, the understanding and the appropriate choice of Dirichlet boundary conditions are the most essential ingredients of the global crack tracking scheme to ensure physically meaningful solutions.

Remark 13 (Invertibility of the anisotropy tensor)

To solve the discrete system of Equations (22), the global system matrix \mathbf{K} needs to be inverted. As the anisotropy tensor \mathbf{D} introduced in Equation (19) is rank deficient, we apply slight perturbations ε as $\mathbf{D} = \mathbf{T}_{\bar{x}} \otimes \mathbf{T}_{\bar{x}} + \mathbf{T}_{\bar{y}} \otimes \mathbf{T}_{\bar{y}} + \varepsilon \mathbf{I}$ to ensure that the overall system is solvable.

Remark 14 (Integration into commercial finite element codes)

Although this algorithm has been termed global tracking algorithm it involves only local modifications on the element level. It is extremely attractive from a practical point of view as the scalar-valued global degrees of freedom ϕ can be treated as the temperature in Fourier’s heat conduction or as the concentration in Fick’ian diffusion in any standard commercial finite element program. Moreover, the algorithm is in principle able to handle multiple cracking. Owing to its computational simplicity, it is extremely robust and stable and highly efficient.

We demonstrate the essential features of the global tracking algorithm in terms of the classical benchmark of the L-shaped concrete panel displayed in Figure 11. This geometry was elaborated experimentally by Winkler *et al.* [46]. Previous discrete failure simulations of this classical benchmark problem can be found, e.g. in Dumstorff and Meschke [43]. However, their analysis is restricted to a two-dimensional setting. The L-shaped panel represents a typical example of curved

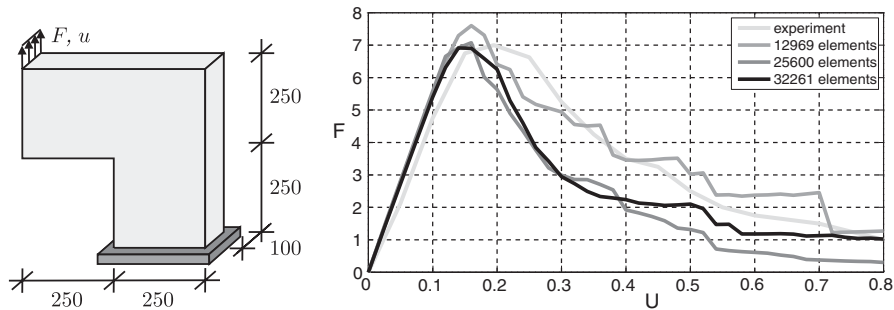


Figure 11. L-shaped panel—Geometry and load–displacement curves for global tracking algorithm.

cracking that could neither be tackled by the local nor by the non-local tracking algorithm. Obviously, the fixed tracking algorithm cannot be applied either as the failure surface is not known in advance. Accordingly, the global tracking algorithm is the only strategy that could potentially be used to simulate the curved failure surface of the L-shaped panel.

The Lamé parameters are $\lambda=6161\text{ N/mm}^2$ and $\mu=10953\text{ N/mm}^2$, the tensile strength is $f_n=2.7\text{ N/mm}^2$, the fracture toughness is $G_n=0.065\text{ N/mm}$ and the shear stiffness is zero $E_t=0\text{ N/mm}$. The domain has been discretized with 12 969, 25 600 and 32 261 linear tetrahedral elements, respectively. The load is applied incrementally through displacement control, i.e. the upper left row of nodes is displaced by $u=0.02\text{ mm}$ in each load steps. The corresponding load–displacement curves and the reference solution to the experimental investigation are displayed in Figure 11 (left). Again, the solution is truly mesh independent and in remarkably good agreement with the experimental reference curve. Figure 12 shows the stress distribution plotted on the deformed configuration. The displayed analysis is based on the discretization with 32 261 linear tetrahedral elements and shows the results of load steps 10 and 20, i.e. at an applied deformation of $u=0.2$ and 0.4 mm , respectively. The crack is initiated at the lower corner element. As the load is increased, the crack propagates smoothly to the right edge of the specimen. Figure 13 shows the

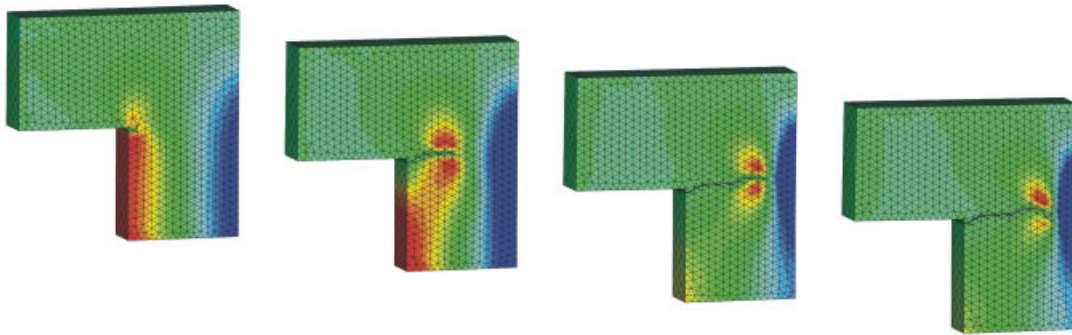


Figure 12. L-shaped panel—Cauchy stress on deformed configuration for load steps 5, 10, 15 and 20 for global tracking algorithm.

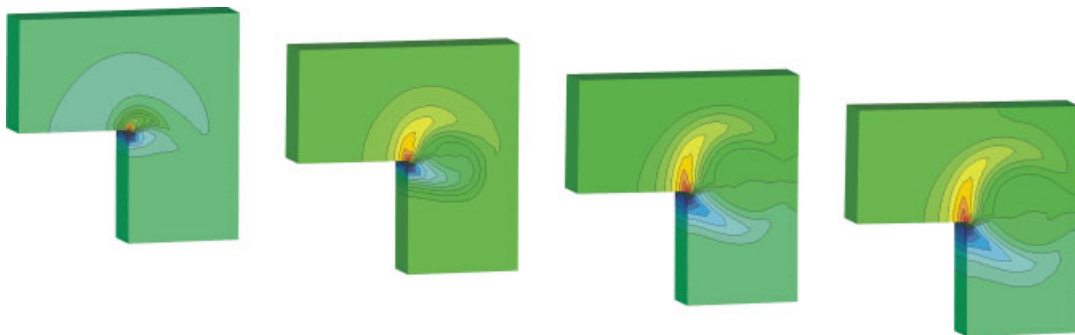


Figure 13. L-shaped panel—Isosurfaces for load steps 5, 10, 15 and 20 for global tracking algorithm.

corresponding isosurfaces $\phi(\mathbf{X}) = \phi_{\mathcal{S}\phi} = \text{const}$ at load steps 10 and 20. The discrete failure surface is clearly visible. In our simulation, it corresponds to the isosurface of level zero, i.e. $\phi(\mathbf{X}) = 0$, but in general, this value can be chosen arbitrarily.

Remarkably, the crack surface is now no longer planar. This example of the cracked L-shaped panel has nicely demonstrated the ability of the global crack tracking scheme to simulate the propagation of curved failure surfaces. It nicely produces smooth \mathcal{C}^0 -continuous arbitrarily shaped discontinuity surfaces, however, at the extra cost of solving an additional linear global system of equations for the values ϕ of the isosurface as scalar-valued nodal unknown. As the coupling of the deformation field $\boldsymbol{\varphi}$ and the isosurface value field ϕ is rather weak, a staggered solution scheme as the one presented herein seems to be favorable over a fully coupled simultaneous solution strategy.

7. EXAMPLES

Finally, we will compare the fixed, local, non-local and global tracking algorithm in terms of two representative examples. Unfortunately, neither the local nor the non-local crack tracking algorithm is particularly well suited to simulate curved cracks. Accordingly, we chose to compare the algorithmic performance in terms of a straight crack problem: the classical three-point bending test. Then, we explore a rectangular block under asymmetric tension inducing a curved failure surface.

7.1. Straight crack—three-point bending test

The first example consists of a simply supported beam loaded by an imposed displacement at the center of its top, see Figure 14. The Lamé parameters are $\lambda = 0 \text{ N/mm}^2$ and $\mu = 50 \text{ N/mm}^2$, the tensile strength is $f_n = 0.1 \text{ N/mm}^2$, the fracture toughness is $G_n = 0.1 \text{ N/mm}$ and the shear stiffness is zero $E_t = 0 \text{ N/mm}$. We apply a Rankine-type crack propagation criterion as introduced in Equation (12), however, as suggested in Section 2.6, we perform the underlying eigenvalue analysis in terms of the non-local rather than the local stress. Cauchy stresses are thus averaged in a certain neighborhood \mathcal{S}^σ around the currently analyzed crack point. Here, we assume that the radius of the averaging sphere to be three times the average element length. The same value is applied for the radius r^{crk} in the non-local crack tracking algorithm that essentially defines the

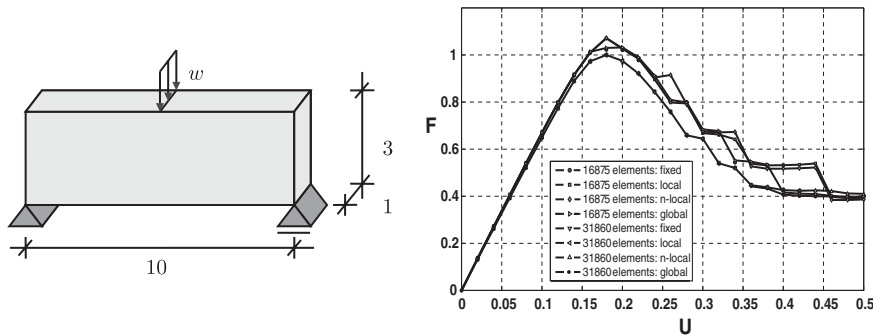


Figure 14. Three-point bending test—Geometry and load–displacement curves for all four algorithms.

averaging set \mathcal{J}^{crk} for the corresponding crack plane normal. Two different structured meshes with 16 875 and 31 860 elements are analyzed. Failure is initialized at the center of the lower face of the beam. As expected, due to the symmetric setup the crack path propagates straight upwards in all four cases. As the discontinuity propagates, we typically observe a change from mode I to mixed mode failure. To overcome the related numerical difficulties we choose to bound the crack deviation angle to 45° .

The corresponding load–displacement curves for the coarse 16 875 element mesh and the finer 31 860 element mesh are displayed in Figure 14 for both the fixed, the local, the non-local and the global crack tracking algorithm. Obviously, the response is independent of the applied crack tracking strategy. The proposed failure criterion depends on the maximum tensile strength of all elements within an averaging sphere that has a radius of three times the average element length. Accordingly, the larger elements of the coarse mesh fail slightly later and the peak load is a little overestimated for the coarse discretization, see Figure 14. Apart from this effect, the good agreement of the eight curves confirms the objectivity of both methods with respect to the discretization.

Furthermore, these results are in good agreement with the solutions to the three-point bending beam analyzed in two dimensions, see e.g. [9, 12, 16]. Figure 15 displays the Cauchy stresses on the deformed configuration at load steps 20, 40 and 80 for all four algorithms. In addition, Figure 16 displays the solution for the second global field of the global tracking algorithm, i.e. the corresponding isosurfaces for load steps 20, 40 and 80. Even though the resulting load–displacement

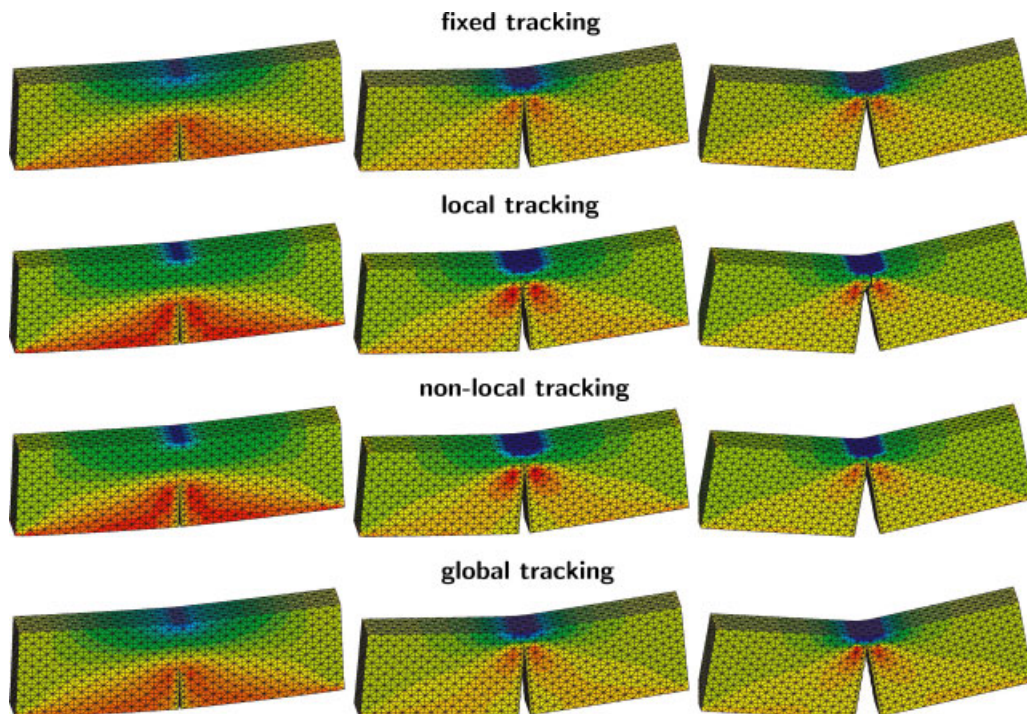


Figure 15. Three-point bending test—Cauchy stresses on deformed configuration for load steps 20, 40 and 80 of all fixed, local, non-local and global algorithm.

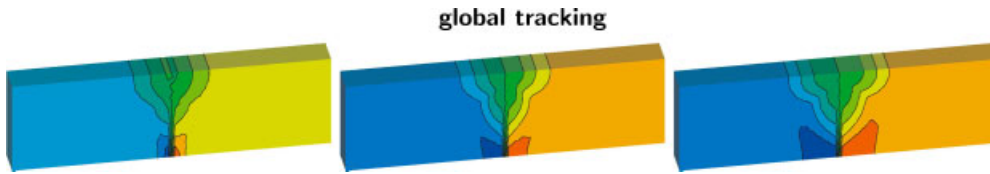


Figure 16. Three-point bending test—Isosurfaces for load steps 20, 40 and 80 for global tracking algorithm.

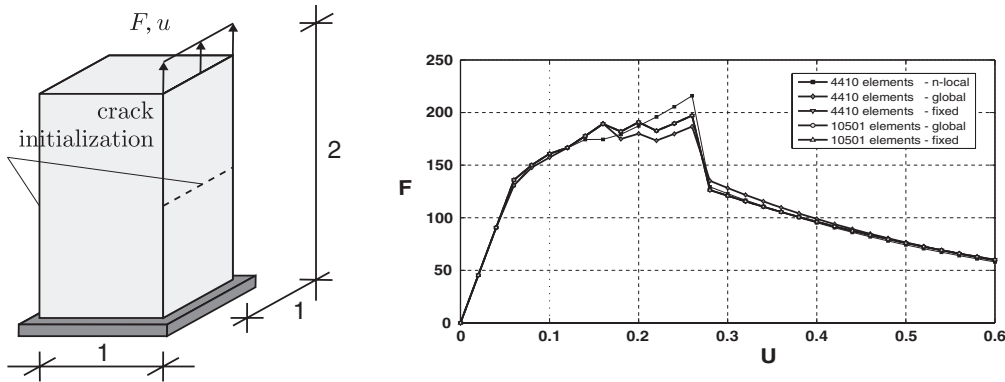


Figure 17. Rectangular block under tension—Geometry and load–displacement curves for all four algorithms.

curves are nearly similar for the four different tracking strategies, the resulting crack surfaces reveal slight differences. They are free of jumps and thus \mathcal{C}^0 -continuous for the fixed, local and global tracking scheme, whereas small jumps at the inter-element boundaries and a \mathcal{C}^{-1} -continuous failure surface are present for the non-local tracking strategy. For this particular example, however, these jumps are yet too small to be seen but they would become visible at a larger magnification.

7.2. Curved crack—rectangular block under tension

First, we analyze the failure of a rectangular block subjected to prescribed incremental displacement of 0.01 mm on one of the top edges, see Figure 17. The block has a square cross section of 1 mm² and a height of 2 mm. It is fixed on the bottom and loaded by a line load on its upper right-hand side. Failure is initiated on the loaded side of the specimen inducing a curved crack surface. The material parameters are chosen to $\lambda=577\text{ N/mm}^2$, $\mu=385\text{ N/mm}^2$, $G_f=100\text{ N/mm}$, $f_t=200\text{ N/mm}^2$, $r_\sigma=2l_{el}$, $r_{crk}=2l_{el}$, with l_{el} being the average element length. In order to compare the prescribed algorithms, the computation is carried out with two different structured meshes, containing 4410 and 10501 elements. For this example, it is essential that an initial crack surface exist when the algorithm starts. Accordingly, we fixed the crack plane normal \mathbf{N} for the first row of initially cracked elements. For the sake of comparison, this crack initiation is applied for all methods. After the crack has propagated about two-thirds of the block, the limit criterion of the local tracking algorithm is met, i.e. the intersection points of the adjacent elements no longer lie within one plane. Accordingly, the local crack tracking algorithm fails to represent the correct

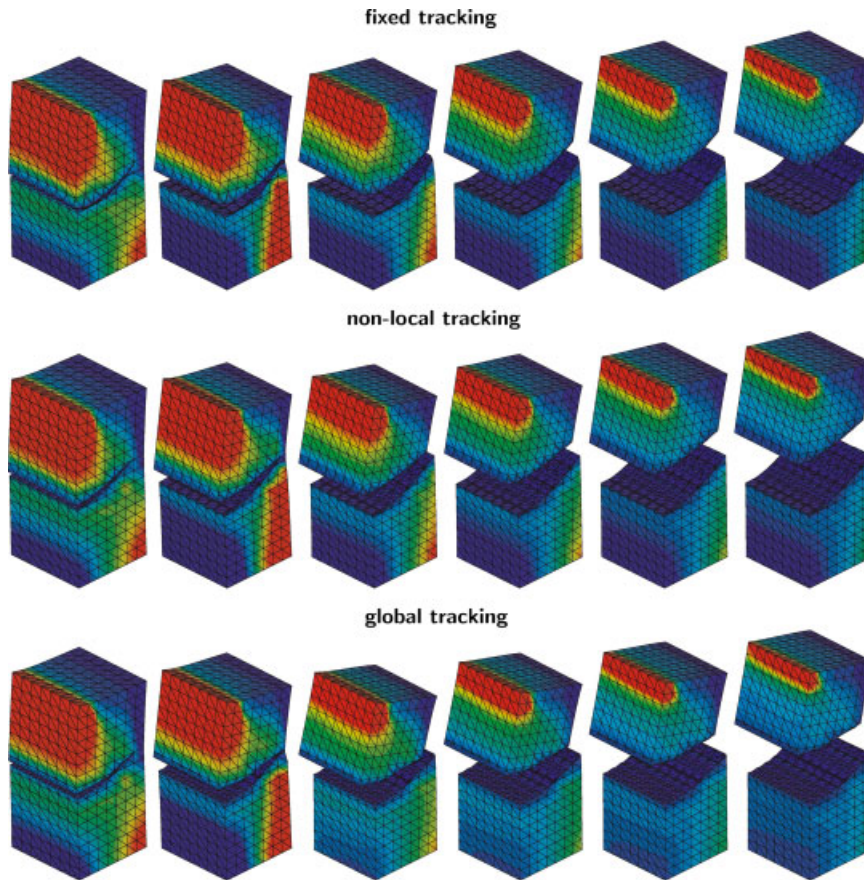


Figure 18. Rectangular block under tension—Cauchy stresses on deformed configuration for load steps 10, 20, 30, 40, 50 and 60 of fixed, non-local and global algorithm.

failure pattern. The load–displacement curves for all other algorithms are depicted in Figure 17. Thereby we have used an imposed parabolic crack path for the fixed tracking algorithm to reproduce and compare the results of the two other algorithms. Figure 18 displays the corresponding the deformed configurations for load steps 10, 20, 30, 40, 50 and 60 for the fixed, non-local and global tracking algorithm. Again, the solution to the second field for the global tracking algorithm is depicted separately in Figure 19. In summary, the four different algorithms have demonstrated mesh-independent performance and yield identical results.

8. DISCUSSION

Four conceptually different strategies for the algorithmic treatment of three-dimensional failure phenomena have been discussed. All four schemes are essentially based on a purely deformation-based Hansbo-type finite element interpolation of the discrete failure surface. Although they apply

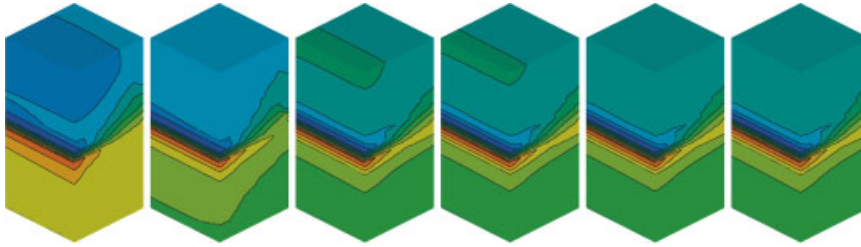


Figure 19. Rectangular block under tension—Isosurfaces for load steps 10, 20, 30, 40, 50 and 60 for global tracking algorithm.

Table II. Comparison of fixed, local, non-local and global crack tracking scheme in terms of computational cost, generality and crack surface continuity.

Tracking	Crack plane normal		Crack surface		Continuity	
Fixed	Prescribed		<i>A priori</i> known	–	$\mathcal{C}^{-1}/\mathcal{C}^0$	+
Local	Neighbor dependent	+	Planar and slightly kinked	–	\mathcal{C}^0	+
Non-local	Non-locally averaged	–	Slightly curved	+	\mathcal{C}^{-1}	–
Global	Unknown d.o.f.	–	Arbitrarily shaped	+	\mathcal{C}^0	+

a discretization that is slightly different from the one applied in classical extended finite element schemes, the four different crack tracking strategies underlying the four algorithms could equally well be combined with the extended finite element method as such. Table II summarizes the outcome of the comparative analysis in terms of computational cost, generality and crack surface continuity.

First of all, we would like to state that all four strategies have been applied successfully to produce mesh-independent results, i.e. provided that the underlying discretization is sufficiently fine, the algorithmic response does not become more brittle with increased mesh refinement. As expected, the fixed crack tracking turned out to be the computationally cheapest and most robust technique to trace discrete failure. It is able to capture \mathcal{C}^0 -continuous planar and curved crack paths provided that the failure surface is *a priori* known. For problem classes with pre-defined weak material interfaces, joints or welding zones, the fixed tracking strategy should, of course, be the method of choice.

For problem classes in which the propagating discontinuity surface is not *a priori* known but rather a part of the solution itself, either the local, the non-local or the global crack tracking strategy can be applied. Ideally, the failure surface should then be a function of the stress state, e.g. the crack plane normal could be chosen as the eigenvector related to the largest eigenvalue of either the local or the non-local Cauchy stress. For two-dimensional crack propagation phenomena, a purely stress-driven crack propagation criterion seems to be the natural choice as it renders a unique smooth crack surface. In that sense, the local crack tracking algorithm can be interpreted as the three-dimensional counterpart of most existing two-dimensional crack propagation schemes. The crack is treated locally as an extension of the existing crack surface on the element level. Starting

from the crack intersection points of the neighboring element, the crack propagates smoothly based on the principal stress direction with slight adjustments based on the neighboring crack points. It is quite obvious that this local crack tracking strategy always produces \mathcal{C}^0 -continuous failure surfaces at extremely low computational cost. Unfortunately, however, these surfaces might eventually be over-constrained in the case of too many pre-existing neighbor crack points. Accordingly, the failure surface typically hardly deviates from a planar or slightly kinked crack path and the structural stiffness would be severely overestimated. In summary, if the failure surface is expected to be rather planar or only slightly kinked, we would advise to use the stable, cheap and robust local crack tracking scheme. In all other cases, a non-local or global tracking scheme should be applied.

To predict failure surfaces of arbitrary shape, the discrete failure surface introduced on the element level essentially needs to incorporate information of the surrounding elements. Within a finite element setting, there are two fundamentally different ways to carry information of a certain neighborhood to the element or rather the integration point level. The first method smoothes the failure surface in a least-squares sense based on the non-locally averaged information within a certain neighborhood. This method is local in the sense that it does not introduce additional global degrees of freedom. Accordingly, however, the generated failure surfaces might show slight jumps at the inter-element boundaries. The non-local crack tracking scheme might be computationally cheaper than the global one as it does not rely on the solution of an additional system of equations. Nevertheless, its underlying algorithmic changes are quite cumbersome and integration into commercial finite element codes would require sophisticated modifications on the integration point level, on the element level and on the system level.

An alternative strategy that is somewhat more tailored to the notion of finite elements is the global crack tracking scheme. At the expense of introducing an additional scalar-valued field of unknowns and having to invert the related system matrix, the global tracking scheme is the only one that really combines advantages of all the previous schemes. It is robust and stable, it is able to reliably capture smooth, curved, arbitrarily shaped \mathcal{C}^0 -continuous failure surfaces and it is straightforwardly integratable into commercial finite element codes. The global crack tracking strategy is the most general of all analyzed schemes and thus applicable in all cases where the failure surface is not *a priori* known and not necessarily expected to be planar.

A comprehensive series of numerical benchmark tests for all four schemes has been performed but only illustrative examples have been presented in this article. The incorporation of the suggested crack tracking strategies into commercial finite element codes that will ultimately allow for more realistic large-scale computations is part of this research. Based on our preliminary studies, however, we believe that especially the global crack tracking strategy has great potential to successfully predict discrete failure phenomena in various kinds of industrially relevant applications and would therefore strongly advocate to incorporate it in commercial finite element codes in the near future.

ACKNOWLEDGEMENTS

This work is part of the research project carried out within the DFG Graduate School 814 'Engineering materials on different scales'. We would kindly like to acknowledge its support through the German National Science Foundation. Moreover, we would like to thank Thomas Christian Gasser for his intensive detailed discussions and helpful advice.

REFERENCES

1. Armero F, Garikipati K. An analysis of strong discontinuities in multiplicative finite strain plasticity and their relation with the numerical simulation of strain localization in solids. *International Journal of Solids and Structures* 1996; **33**(20–22):2863–2885.
2. Dvorkin EN, Cuitino AM, Gioia G. Finite-elements with displacement interpolated embedded localization lines insensitive to meshsize and distortions. *International Journal for Numerical Methods in Engineering* 1990; **30**(3):541–564.
3. Oliver J. Modelling strong discontinuities in solid mechanics via strain softening constitutive equations. 1. Fundamentals. *International Journal for Numerical Methods in Engineering* 1996; **39**(21):3575–3600.
4. Oliver J. Modelling strong discontinuities in solid mechanics via strain softening constitutive equations. 2. Numerical simulation. *International Journal for Numerical Methods in Engineering* 1996; **39**(21):3601–3623.
5. Sluys LJ, Berend AH. Discontinuous failure analysis for mode-I and mode-II localization problems. *International Journal of Solids and Structures* 1998; **35**(31–32):4257–4274.
6. Simo JC, Armero F, Taylor RL. Improved versions of assumed enhanced strain tri-linear elements for 3D-finite deformation problems. *Computer Methods in Applied Mechanics and Engineering* 1993; **110**(3–4):359–386.
7. Belytschko T, Moës M, Usui S, Parimi C. Arbitrary discontinuities in finite elements. *International Journal for Numerical Methods in Engineering* 2001; **50**(4):993–1013.
8. Dolbow J, Moës N, Belytschko T. Discontinuous enrichment in finite elements with a partition of unity method. *Finite Elements in Analysis and Design* 2000; **36**(3–4):235–260.
9. de Borst R. Numerical aspects of cohesive-zone models. *Engineering Fracture Mechanics* 2003; **70**(14):1743–1757.
10. de Borst R, Guitierrez MA, Wells GN, Remmers JC, Askes H. Cohesive-zone models, higher-order continuum theories and reliability methods for computational failure analysis. *International Journal for Numerical Methods in Engineering* 2004; **60**(1):289–315.
11. Remmers JJC, de Borst R, Needleman A. A cohesive segments method for the simulation of crack growth. *Computational Mechanics* 2003; **31**(1–2):69–77.
12. Wells GN, Sluys LJ. A new method for the modelling of cohesive cracks using finite elements. *International Journal for Numerical Methods in Engineering* 2001; **50**(12):2667–2682.
13. Wells GN, Sluys LJ, de Borst R. Simulating the propagation of displacement discontinuities in a regularized strain-softening medium. *International Journal for Numerical Methods in Engineering* 2002; **53**(5):1235–1256.
14. Hansbo A, Hansbo P. A finite element method for the simulation of strong and weak discontinuities in solid mechanics. *Computer Methods in Applied Mechanics and Engineering* 2004; **193**(33–35):3532–3540.
15. Hansbo A, Hansbo P, Larson MG. A finite element method on composite grids based on Nitsche's method. *ESAIM: Mathematical Modelling and Numerical Analysis* 2003; **37**(3):495–514.
16. Kuhl E, Jäger P, Mergheim J, Steinmann P. On the application of Hansbo's method for interface problems. In *Proceedings of the IUTAM Symposium on Discretization Methods for Evolving Discontinuities*, Lyon, France, Combescure A, de Borst R, Belytschko T (eds). Springer: Berlin, 2006.
17. Mergheim J, Kuhl E, Steinmann P. A hybrid discontinuous Galerkin/interface method for the computational modelling of failure. *Communications in Numerical Methods in Engineering* 2004; **20**(7):511–519.
18. Mergheim J, Kuhl E, Steinmann P. A finite element method for the computational modelling of cohesive cracks. *International Journal for Numerical Methods in Engineering* 2005; **63**(2):276–289.
19. Mergheim J, Kuhl E, Steinmann P. Towards the algorithmic treatment of 3D strong discontinuities. *Communications in Numerical Methods in Engineering* 2007; **23**(2):97–108.
20. Areias PMA, Belytschko T. A comment on the article 'A finite element method for the simulation of strong and weak discontinuities in solid mechanics' by A. Hansbo and P. Hansbo [*Computer Methods in Applied Mechanics and Engineering* 2004; **193**:3523–3540]. *Computer Methods in Applied Mechanics and Engineering* 2006; **195**(9–12):1275–1276.
21. Areias PMA, Song JH, Belytschko T. Analysis of fracture in thin shells by overlapping paired elements. *Computer Methods in Applied Mechanics and Engineering* 2006; **195**(41–43):5343–5360.
22. Jäger P, Steinmann P, Kuhl E. On local tracking algorithms for the simulation of three-dimensional discontinuities. *Computational Mechanics* 2007; DOI: 10.1007/s00466-008-0249-3.
23. Meschke G, Dumstorff P. Energy-based modeling of cohesive and cohesionless cracks via X-FEM. *Computer Methods in Applied Mechanics and Engineering* 2007; **196**(21–24):2338–2357.
24. Areias PMA, Belytschko T. Analysis of three-dimensional crack initiation and propagation using the extended finite element method. *International Journal for Numerical Methods in Engineering* 2005; **63**(5):760–788.

25. Chaves EWW. Tracking 3D crack path. *Proceedings of the International Conference on Mathematical and Statistical Modeling in Honor of Enrique Castillo*. ICMSM Ciudad Real: Spain, 2006.
26. Feist C, Hofstetter G. Three-dimensional fracture simulations based on the SDA. *International Journal for Numerical and Analytical Methods in Geomechanics* 2007; **31**(2):189–212.
27. Gasser TC, Holzapfel GA. Modeling 3D crack propagation in unreinforced concrete using PUFEM. *Computer Methods in Applied Mechanics and Engineering* 2005; **194**(25–26):2859–2896.
28. Gasser TC, Holzapfel GA. 3D Crack propagation in unreinforced concrete. A two-step algorithm for tracking 3D crack paths. *Computer Methods in Applied Mechanics and Engineering* 2006; **195**(37–40):5198–5219.
29. Gasser TC. Validation of 3D crack propagation in plain concrete. Part II: computational modeling and predictions of the PCT3D test. *Computers and Concrete* 2007; **4**(1):67–82.
30. Gravouil A, Moës N, Belytschko T. Non-planar 3D crack growth by the extended finite element and level sets—Part II: level set update. *International Journal for Numerical Methods in Engineering* 2002; **53**(11):2569–2586.
31. Mosler J, Meschke G. 3D modelling of strong discontinuities in elastoplastic solids: fixed and rotating localization formulations. *International Journal for Numerical Methods in Engineering* 2003; **57**(11):1553–1576.
32. Mosler J. Modeling strong discontinuities at finite strains—a novel numerical implementation. *Computer Methods in Applied Mechanics and Engineering* 2006; **195**(33–36):4396–4419.
33. Moës N, Gravouil A, Belytschko T. Non-planar 3D crack growth by the extended finite element and level sets—Part I: mechanical model. *International Journal for Numerical Methods in Engineering* 2002; **53**(11):2549–2568.
34. Oliver J, Huespe AE. On strategies for tracking strong discontinuities in computational failure mechanics. In *Proceedings of the Fifth World Congress on Computational Mechanics (WCCM V)*, Vienna, Austria, Mang HA, Rammendorfer FG, Erberhardsteiner J (eds). 2002.
35. Pandolfi A, Ortiz M. An efficient adaptive procedure for three-dimensional fragmentation simulations. *Engineering Computations* 2002; **18**(2):148–159.
36. Rabczuk T, Belytschko T. A three dimensional large deformation meshfree method for arbitrary evolving cracks. *Computer Methods in Applied Mechanics and Engineering* 2007; **196**:2777–2799.
37. Ruiz G, Ortiz M, Pandolfi A. Three-dimensional finite-element simulation of the dynamic Brazilian tests on concrete cylinders. *International Journal for Numerical Methods in Engineering* 2000; **48**(7):963–994.
38. Sancho JM, Planas J, Fathy AM, Galvez JC, Cendon DA. Three-dimensional simulation of concrete fracture using embedded crack elements without enforcing crack path continuity. *International Journal for Numerical and Analytical Methods in Geomechanics* 2007; **31**(2):173–187.
39. Sukumar N, Moës N, Moran B, Belytschko T. Extended finite element method for three-dimensional crack modelling. *International Journal for Numerical Methods in Engineering* 2000; **48**(11):1549–1570.
40. Feist C, Hofstetter G. Crack propagation in plain concrete. Part I: experimental investigation—the PCT3D test. *Computers and Concrete* 2007; **4**(1):49–66.
41. Oliver J, Huespe AE, Samaniego E, Chaves EVW. Continuum approach to the numerical simulation of material failure in concrete. *International Journal for Numerical and Analytical Methods in Geomechanics* 2004; **28**(7–8):609–632.
42. Cervera M, Chiumenti M. Mesh objective tensile cracking via a local continuum damage model and a crack tracking technique. *Computer Methods in Applied Mechanics and Engineering* 2006; **196**(1–3):304–320.
43. Dumstorff P, Meschke G. Crack propagation criteria in the framework of X-FEM-based structural analyses. *International Journal for Numerical and Analytical Methods in Geomechanics* 2007; **31**(2):239–259.
44. Jirasek M, Rolshoven S, Grassl P. Size effects on fracture energy induced by non-locality. *International Journal for Numerical and Analytical Methods in Geomechanics* 2004; **28**(7–8):653–670.
45. Feist C, Hofstetter G. An embedded strong discontinuity model for cracking of plain concrete. *Computer Methods in Applied Mechanics and Engineering* 2006; **195**(52):7115–7138.
46. Winkler BJ, Hofstetter G, Niederwanger G. Experimental verification of a constitutive model for concrete cracking. *Proceedings of the Institution of Mechanical Engineers, Part L: Journal of Materials—Design and Applications* 2001; **215**(L2):75–86.